

Spin-Valley Protected Kramers Pair in Bilayer Graphene

Artem O. Denisov,^{1,*} Veronika Reckova,¹ Solenn Cances,¹ Max J. Ruckriegel,¹
Michele Masseroni,¹ Christoph Adam,¹ Chuyao Tong,¹ Jonas D. Gerber,¹ Wei Wister Huang,¹
Kenji Watanabe,² Takashi Taniguchi,³ Thomas Ihn,^{1,4} Klaus Ensslin,^{1,4} and Hadrien Duprez^{1,†}

¹Laboratory for Solid State Physics, ETH Zurich, CH-8093 Zurich, Switzerland

²Research Center for Functional Materials, National Institute for Materials Science, 1-1 Namiki, Tsukuba 305-0044, Japan

³International Center for Materials Nanoarchitectonics,

National Institute for Materials Science, 1-1 Namiki, Tsukuba 305-0044, Japan

⁴Quantum Center, ETH Zürich, CH-8093 Zürich, Switzerland

The intrinsic valley degree of freedom makes bilayer graphene (BLG) a unique platform for semiconductor qubits. The single-carrier quantum dot (QD) ground state exhibits a two-fold degeneracy, where the two states that constitute a Kramers pair, have opposite spin and valley quantum numbers. Because of the valley-dependent Berry curvature, an out-of-plane magnetic field breaks the time-reversal symmetry of this ground state and a qubit can be encoded in the spin-valley subspace. The Kramers states are protected against known spin- and valley-mixing mechanisms because mixing requires a simultaneous change of both quantum numbers. Here, we fabricate a tunable QD device in Bernal BLG and measure a spin-valley relaxation time for the Kramers states of 38 s, which is two orders of magnitude longer than the 0.4 s measured for purely spin-blocked states. We also show that the intrinsic Kane-Mele spin-orbit splitting enables a Kramers doublet single-shot readout even at zero magnetic field with a fidelity above 99%. If these long-lived Kramers states also possess long coherence times and can be effectively manipulated, electrostatically defined QDs in BLG may serve as long-lived semiconductor qubits, extending beyond the spin qubit paradigm.

Atomically thin semiconductors with a hexagonal crystal lattice serve as a unique host for solid-state qubits [1, 2] due to their intrinsic valley degree of freedom. Among them, bilayer graphene stands out as a platform that benefits from carbon’s low nuclear spin density and weak spin-orbit coupling, along with the ability to fabricate highly tunable few-carrier quantum dots [3–5]. The two-fold valley degeneracy [6, 7] provides an opportunity to define a qubit in the two-dimensional subspace spanned by the valley and the spin degrees of freedom [8]. One benefit of encoding a qubit using two quantum numbers instead of one is its robustness (protection) against different types of noise that would otherwise cause it to decay. While the spin is coupled to surrounding magnetic moments and phonons via spin-orbit coupling (SOC) [9] or hyperfine interaction [10], a valley flip requires a scattering process with a giant momentum swing on the order of

the length of the reciprocal lattice vector, which is only known to be caused by short-range perturbations on the length scale of atomic defects. Given the low disorder reached in encapsulated graphene [11], the valley relaxation times were demonstrated to be at least an order of magnitude longer than spin relaxation times [3] within a single device. One can speculate that the simultaneous flip of both spin and valley [12], thus, is a rare second-order process.

A remarkable property of BLG is a large out-of-plane valley g -factor (g_v), which originates from the finite Berry curvature around the K -points [13] and can be tuned using the electric field across a wide range of values from 10 to 100 [14]. At zero magnetic field, the four-fold single-particle degeneracy is already lifted by Kane–Mele spin–orbit interaction [15]. It separates the energy of the two Kramers doublets ($|K^-\uparrow\rangle$, $|K^+\downarrow\rangle$) and ($|K^-\downarrow\rangle$, $|K^+\uparrow\rangle$) by a spin-orbit gap, which has been previously measured indirectly [16–18] and directly [17, 19] to be $\Delta_{\text{SO}} \approx 40 - 80 \mu\text{eV} \cong 10 - 20 \text{ GHz}$. Comparable spin-orbit splittings are observed between Kramers pairs in semiconducting transition metal dichalcogenide (TMD) multilayer systems, such as MoS_2 [12]. By increasing B_\perp , time-reversal symmetry is broken resulting in an energy splitting of both Kramers pairs. Previous studies showed coherent oscillations of a spin–valley qubit formed in a carbon nanotube (CNT) [20] but yielded short relaxation times $T_1 < 10 \mu\text{s}$ [20, 21] and decoherence times $T_2^{(\text{echo})} = 65 \text{ ns}$ presumably attributed to high levels of static disorder and charge noise [20–22]. In contrast, encapsulated BLG is known to be atomically flat, and with significantly slower valley mixing rate $\Delta_{K^+K^-} < 2 \text{ neV}$ [3], promising longer relaxation times.

In this work, we perform relaxation time measurements of a single-hole quantum dot formed in BLG with small ($\sim \text{mT}$) or zero applied magnetic field. We find the relaxation time T_1 for simultaneous spin–valley relaxation to be as long as $T_1^{(\text{sv})} \approx 30 \text{ s}$ which is two orders of magnitude longer than for pure spin relaxation $T_1^{(\text{s})} \approx 0.4 \text{ s}$. Additionally, we demonstrate high fidelity readout at zero magnetic field where relaxation happens between two Kramers doublets and requires either a spin or a valley flip.

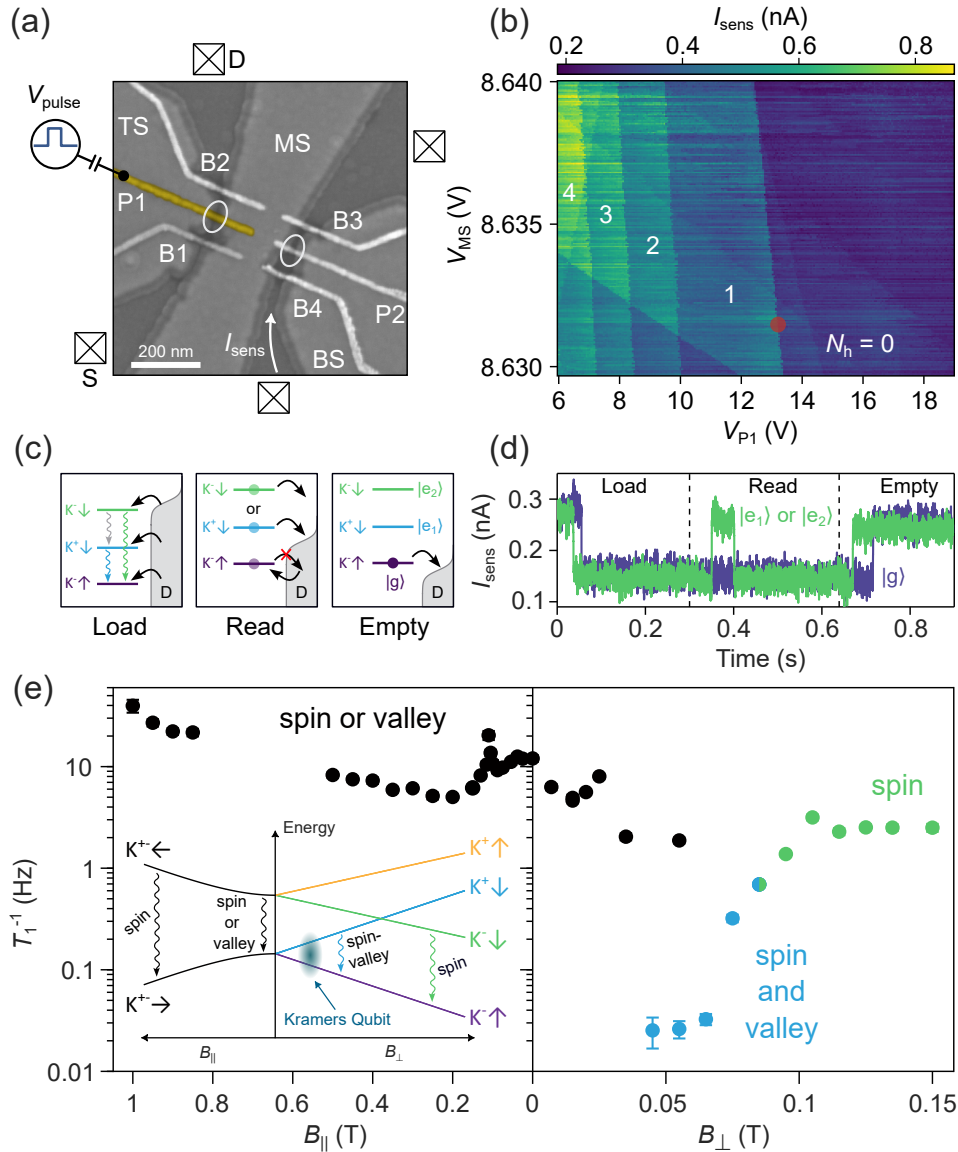


FIG. 1. Device and pulsing protocol used to determine relaxation times. (a) SEM false-color image of the device. All labeled metallic gates – including barrier gates (B1-B4), plunger gates (P1, P2), split gates (TS, MS, BS), and the graphite back gate (not shown) – as well as the source (S) and drain (D) ohmic contacts, are DC-biased. The plunger gate P1 is additionally controlled by AC pulses. (b) Charge stability diagram of the dot probed with a charge sensor current I_{sens} as a function of the middle-split gate V_{MS} and plunger gate V_{P1} voltages. N_h indicates the number of hole carriers inside the QD. The red mark indicates the point on the gate-gate diagram where all measurements were performed. (c) Three-step pulse readout protocol. Schematic energy diagrams for the three lowest states of the single hole in the BLG QD at $B_{\perp} = 40$ mT. (d) Single-shot readout of the hole state. Typical time-traces of the sensor current I_{sens} in response to a three-level pulse. For the green trace, the hole is declared to be in one of the excited states (ESs) by the characteristic current step during the ‘Read’ phase. For the purple trace, the hole is declared to be in the ground state if no step is observed during the ‘Read’ phase. (e) Measured inverse relaxation time T_1^{-1} as a function of in-plane B_{\parallel} and out-of-plane B_{\perp} magnetic fields. Marks of different colors at the same magnetic field correspond to different relaxation channels controlled by changing the amplitude of ‘Load’ and ‘Read’ pulses. Data points are presented as mean values \pm the standard deviation of the calculated T_1 (Methods). Some error bars are smaller than the symbol size of the data point. The inset shows the energy spectrum of a single carrier in the BLG QD plotted as a function of in-plane and out-of-plane magnetic fields.

We form a tunable QD device, electrostatically defined in Bernal BLG, using two layers of overlapping gates depicted in Fig. 1a (see Methods for fabrication details). The lower gate layer serves the purpose of confining the

BLG charge carriers to two conducting channels via opening the band gap in BLG underneath the top (TS), middle (MS), and bottom (BS) split gates, and placing the Fermi energy into the gap in these regions [23]. The up-

per gate layer of narrow finger gates is used to precisely define the QDs within the channels. We form the signal and the sensor QDs underneath their respective plunger gates P1 and P2. The dot-to-reservoir couplings can be tuned individually by pairs of barrier gates (B1, B2) and (B3, B4), respectively. We tune the dot into the single-hole regime as shown in Fig. 1b, where the sensor current I_{sens} is shown as a function of middle split and plunger gate voltages V_{MS} and V_{P1} . From the width of the 0 – 1 charge transition, we determine the electron temperature to be $T_e \approx 30$ mK.

THREE-LEVEL SINGLE-SHOT READOUT

We perform the standard Elzerman three-level single-shot readout [4, 24, 25] to extract the relaxation times (see Methods for the details). We apply voltage pulses to the plunger gate P1, while monitoring the real-time charge occupancy of the dot using the charge sensor. The concept of the readout is sketched in Fig. 1c: if a hole remains in the excited state after the ‘Load’ and during the ‘Read’ phase without relaxing, then, at some random time governed by the tunneling-out rate, it will tunnel to the leads and thereafter the ground state of the dot will be occupied again through a tunneling-in process. This in-and-out tunneling manifests itself as a step in the sensor current shown in Fig. 1d (green trace). By determining the ratio of the number of shots with a single step to the total number of successfully loaded shots and discarding error traces (see Methods for postselection procedure), we extract the relaxation time by fitting the exponential decay as a function of the load time [26].

Figure 1e shows the main results of this paper: the measured relaxation times T_1 are plotted as a function of small out-of-plane and in-plane magnetic fields. As we will prove later by excited state spectroscopy measurements, at $B_{\perp} < 80$ mT, the transition between the two lowest energy states in the single-particle spectrum are spin–valley blocked, so the resulting T_1 times can be interpreted as spin–valley relaxation times $T_1^{(\text{sv})}$ (blue points in the figure). We observed long relaxation times $T_1^{(\text{sv})} \approx 30$ s. This is in tune with the intuition that, a simultaneous flip of both quantum numbers is a very rare second-order relaxation process. Note that the range in magnetic field where we can measure this spin–valley relaxation time is bounded from below by $B_{\perp} \gtrsim 40$ mT and from above by $B_{\perp} \lesssim 70$ mT. We notice, that at lower energy splittings, the fidelity of Elzerman readout drastically drops, affected by finite temperature and charge noise [27]. We would like to note that similarly long T_1 times were measured in GaAs [10] in the limit close to $B = 0$. In both cases the times are probably rather limited by the required measurement time and sample stability than by the two-level system itself.

At low perpendicular magnetic fields, by choosing

the ‘Read’ level such that E_F in the lead is inside the gap between the Kramers pairs, we can perform high-fidelity readout of the pair state and measure relaxation times between two doublets which are blocked by either spin or valley flip (black points in Fig. 1e). As a result, the resulting relaxation time is dominated by the fastest of two channels and can be expressed as $T_1 = (1/T_1^{(\text{s})} + 1/T_1^{(\text{v})})^{-1}$.

Applying a perpendicular magnetic field lifts the Kramers pairs’ degeneracies, and enables us to distinguish the spin and spin–valley relaxation rates by accurately placing the E_F of the lead between the corresponding states. Around $B_{\perp} \approx 80$ mT in Fig. 1e, two excited states cross, namely $|K^{-}\downarrow\rangle$ and $|K^{+}\downarrow\rangle$. For $B_{\perp} > 80$ mT, the transition between the two lowest states, $|K^{-}\downarrow\rangle$ and $|K^{-}\uparrow\rangle$, is purely spin-blocked, meaning that the measured T_1 times can be identified with spin relaxation times $T_1^{(\text{s})}$ (green data points). We measured $T_1^{(\text{s})} \approx 0.4$ s which is two orders of magnitude shorter than the spin–valley relaxation time, but still one order of magnitude longer than spin relaxation times previously measured at higher magnetic fields $B_{\perp} > 1.5$ T [3, 4]. This finding is consistent with phonon spin relaxation mediated by SOC and/or hyperfine coupling [10, 28]. Such long spin T_1 times are also consistent with the fact the QD is highly decoupled from the leads with the intrinsic tunneling rate as low as $\Gamma_{\text{out}} \approx 15$ Hz (see Methods for $\Gamma_{\text{in/out}}$ extraction). Additionally, we find no relaxation hotspot [9, 29] where two different valley states cross (at $B_{\perp} = 80$ mT) in Fig. 1e. This is consistent with the low inter-valley mixing term measured in BLG [3, 19]. In Methods section, we explicitly rule out the argument that the observed long spin–valley relaxation times could be interpreted as fully dominated by pure spin relaxation.

In Fig. 1e left we also show the non-monotonic dependence of the T_1 -time as a function of in-plane magnetic field B_{\parallel} that does not break the Kramers degeneracy but slowly increases the energy splitting of the Kramers pairs. Starting from $T_1 \approx 100$ ms at zero magnetic field, the relaxation time doubles around $B_{\parallel} = 200$ mT and then decreases monotonically at higher fields, reaching $T_1 \approx 25$ ms at $B_{\parallel} = 1$ T. We also observe two insignificant relaxation hotspots around $B_{\parallel} = 110$ mT and $B_{\perp} = 20$ mT. These hotspots leave no traces in spectroscopy measurements (see Supplementary Figure 2).

SINGLE-SHOT EXCITED STATE SPECTROSCOPY

To support the identification of the different relaxation channels discussed above, we carefully probe the state spectrum of our QD by standard ‘Read’ window calibration [25, 29]. In Fig. 2b, we graph the occupation probability of the QD estimated from ~ 140 single shot traces, varying the ‘Read’ level position relative to the

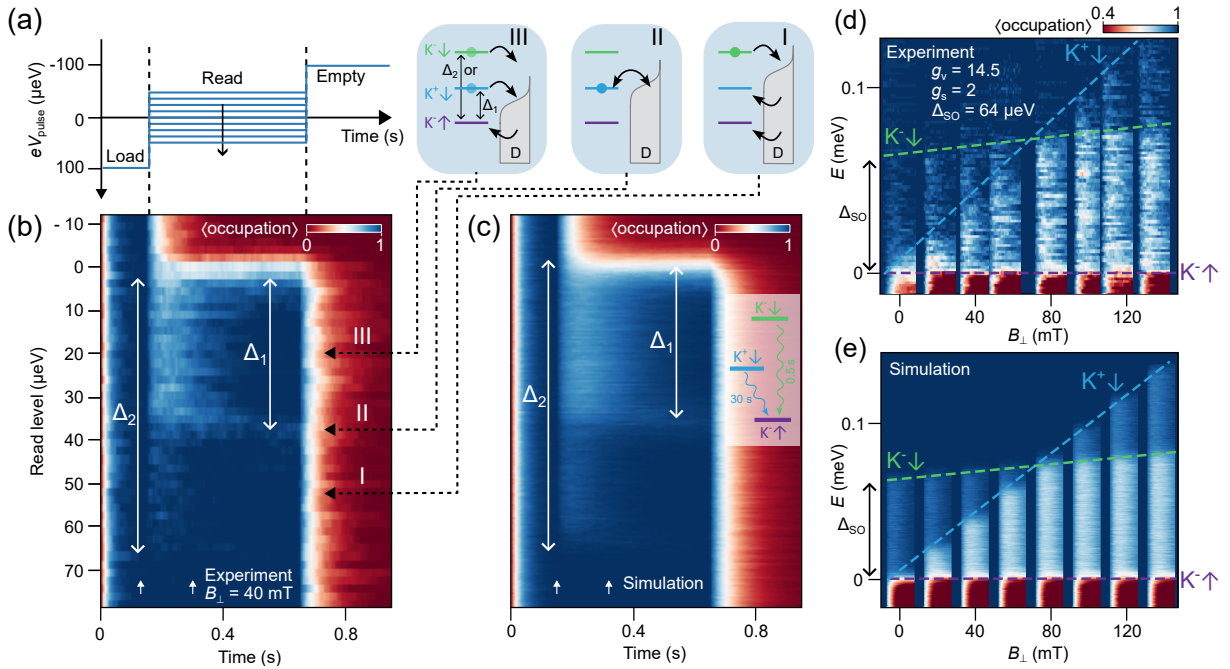


FIG. 2. **Single-shot energy spectroscopy.** (a) Calibration of the ‘Read’ level and the excited state spectroscopy. The ‘Read’ level is varied while the ‘Load’ and ‘Empty’ are kept constant. (b) The digitized sensor current (representing dot occupation) averaged over ~ 140 single-shot traces as a function of the ‘Read’ level shift relative to the GS at $B_{\perp} = 40$ mT. Insets sketch the relative position of the dot’s energy levels and the E_F of the lead for three different regimes: (III) readout from both ESs, (II) resonant jumps between the lower energy ES and the lead, (I) readout from the higher energy ES. Δ_1 and Δ_2 denote the energy splittings between the GS and the two ESs respectively. The sensor signal is digitized to represent the dot occupation, such that current offsets due to the sensor drift are compensated. (c) Monte-Carlo simulation of the single-shot readout averaged over 10,000 shots for each ‘Read’ level. We use the simplest model with three states, as shown on the sketch, where both of the ESs can only relax to the GS with $T_1^{(s)} = 0.5$ s and $T_1^{(sv)} = 30$ s — two values measured independently. (d) Excited state spectroscopy. The beginning of the ‘Read’ phase (spanning the time window marked with white arrows in (b)) is shown for $B_{\perp} = [0, 20, 40, 55, 80, 100, 115, 135]$ mT. The ‘Read’ level shift relative to the GS. The dashed lines show the evolution of the two lower energy ESs in a single-hole BLG QD: $|K^{-}\downarrow\rangle$ (green) and $|K^{+}\downarrow\rangle$ (blue), with $\Delta_{\text{SO}} = 64 \mu\text{eV}$ and $g_v = 14.5$. (e) Similar data as in (d) but for Monte-Carlo simulated single-shot readout of the QD. The averaged step maps do not reveal solid evidence for the existence of the fourth state $|K^{+}\uparrow\rangle$ presumably due to the short relaxation time of the hole in this state. However, we could observe all four non-degenerate states and their predicted magnetic field dependence using more precise tunneling rate spectroscopy measurements [19] as shown in the Supplementary Figure 1. Scale bar is shared with (d).

alignment between the ground state and the Fermi energy in the leads. The ‘Load’ ($eV_{\text{load}} = 95 \mu\text{eV}$) and ‘Empty’ ($eV_{\text{empty}} = -95 \mu\text{eV}$) levels are kept constant during this process (see the sketch in Fig. 2a). The finite probability of having a step in the sensor trace reduces the average dot occupation at the beginning of the ‘Read’ phase as seen from Fig. 2b (light blue region). We can clearly distinguish three different regimes here: (I) Low density of steps between $35 \mu\text{eV}$ and $65 \mu\text{eV}$ as we read out only the higher energy ES $|K^{-}\downarrow\rangle$, (III) high density of steps between 0 and $35 \mu\text{eV}$ as we readout both of the ESs and (II) where the density of steps decays very slowly over time, indicating resonant back-and-forth jumps of the hole between the lower energy ES $|K^{+}\downarrow\rangle$ and the lead as their energies align. In Fig. 2d we plot the beginning of the ‘Read’ phase (within a time-interval indicated by white arrows in Fig. 2b) at different out-of-plane magnetic fields. We clearly observe the predicted [7] crossing

between two ESs around $B_{\perp} \approx 80$ mT. At zero magnetic field, the GS $|K^{-}\uparrow\rangle$ and the first ES $|K^{+}\downarrow\rangle$ form a Kramers pair and B_{\perp} splits it with $\Delta_1 = (g_v + g_s)\mu_B B_{\perp}$. Relaxation of the second ES $|K^{-}\downarrow\rangle$ into the GS is spin-blocked and evolves in B_{\perp} as $\Delta_2 = g_s\mu_B B_{\perp} + \Delta_{\text{SO}}$. The extracted $g_v = 14.5$ (we checked that $g_s = 2$ independently, see Supplementary Figure 1), and the Kane–Mele SO gap $\Delta_{\text{SO}} = 64 \pm 4 \mu\text{eV}$ agree with the previously measured values [16–19].

We can qualitatively compare the data with the results of a simple three state Monte-Carlo model of the single-shot readout [25] (see Supplementary Information, section V for details) with $T_1^{(s)} = 0.5$ s and $T_1^{(sv)} = 30$ s. Figure 2c shows the results of the simulations which aim to qualitatively match the experimental step map in Fig. 2b. As expected, the simulation of the B_{\perp} -dependence in Fig. 2e qualitatively agrees with the experiment in Fig. 2d.

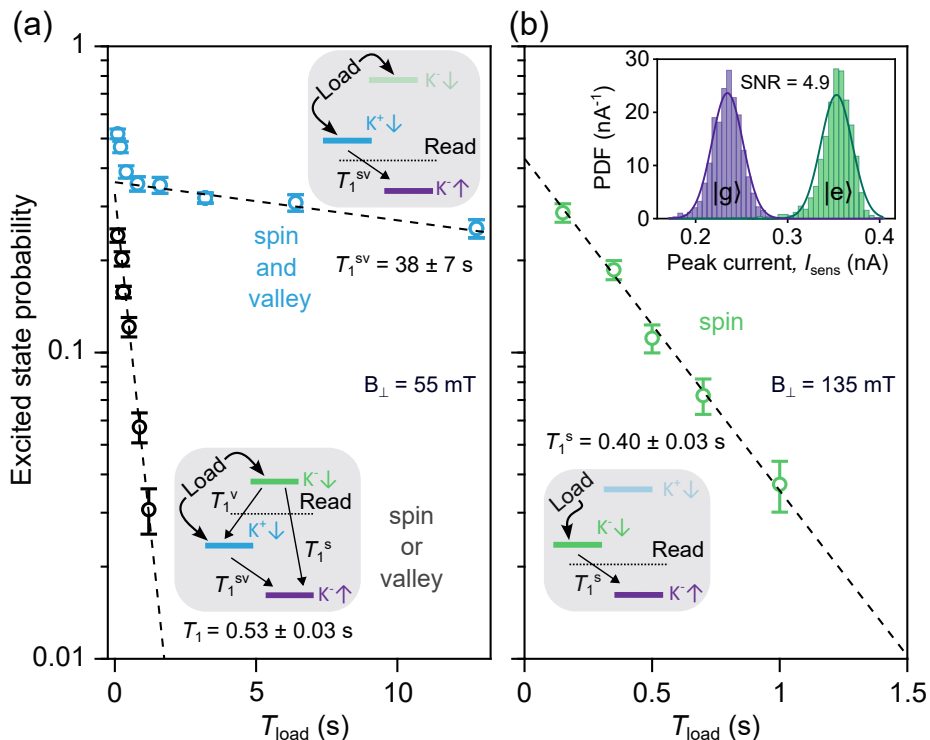


FIG. 3. **Distinguishing different relaxation channels.** (a) Exponential decays of the excited state probability at $B_{\perp} = 55$ mT. The upper sketch shows the measurement of the relaxation time from both ESs in parallel (blue circles). Here, the ‘Read’ level is placed below both of the the ESs and above the GS. The lower sketch depicts the relaxation measurements only from the higher energy ES (black circles). Here, the ‘Read’ level is placed between the first and the second ESs. Dashed lines show the exponential fits with outlined T_1 times. (b) Exponential decay of the ES probability at $B_{\perp} = 135$ mT. The sketch depicts the standard spin readout protocol: the ‘Load’ level is placed between the two ESs, while the ‘Read’ level is placed between the GS and the lower energy ES. The transition between these two states are spin-blocked. Data points in (a) and (b) are presented as mean values \pm the confidence interval of a single standard deviation (Methods). Inset shows a probability density function (PDF) histograms of the maximum values of the sensor current in the ‘Read’ phase extracted separately from the shots where the state at the beginning of the ‘Read’ phase is identified as the ES (green) and the GS (purple). The solid lines are Gaussian fits obtained separately for each histogram.

IDENTIFYING DIFFERENT RELAXATION CHANNELS

We start the discussion on how we access all three types of blockade in Fig. 1e with perpendicular magnetic fields beyond the crossing $B_{\perp} > 80$ mT. Here the relaxation between the first ES $|K^{-}\downarrow\rangle$ and the GS $|K^{-}\uparrow\rangle$ is spin-blocked as depicted in Fig. 3b. During the ‘Read’ phase, the E_F of the lead (represented by the dotted line in Fig. 3a and b) is placed between the GS and first ES to facilitate spin-to-charge conversion. The exponential decay of the spin-down probability in Fig. 3b yields long $T_1^{(s)} = 0.40 \pm 0.03$ s [3, 4].

At lower magnetic fields $B_{\perp} < 80$ mT, the ESs swap their order, and the relaxation between the now lower energy ES $|K^{+}\downarrow\rangle$ and the GS $|K^{-}\uparrow\rangle$ becomes spin-and-valley blocked. Due to the presence of occasional charge jumps, we find it easier to load a hole into both ESs rather than accurately placing the ‘Load’ level between the ESs. The lower sketch in Fig. 3a illustrates the

readout of the higher energy ES $|K^{-}\downarrow\rangle$ which requires a spin or valley flip to relax to the GS or the lower energy ES, respectively. The resulting relaxation rate obtained from the black data points is, therefore, the average of two parallel relaxation channels $T_1 = (1/T_1^{(s)} + 1/T_1^{(v)})^{-1} = 0.53 \pm 0.03$ s, with a value close to the spin relaxation times and likely dominated by it [3]. We want to highlight a key feature in the relaxation measurement of the higher energy ES $|K^{-}\downarrow\rangle$: when loading times exceed $T_{\text{load}} \approx 2$ s, all carriers loaded to the higher energy ES relax, leaving it unoccupied.

Alternatively, we can measure relaxation from both the ESs by moving the ‘Read’ level below the lower energy ES, as shown in the upper sketch in Fig. 3a. Here, two distinct regimes in the exponential decay of the ES probability (blue data points) are evident: at short loading times, the relaxation rate is fast and attributed to the relaxation from the highest ES, while around $T_{\text{load}} > 1$ s, the second regime of rather long relaxation becomes apparent. As we have illustrated that the higher energy

ES is unoccupied at these loading times, we attribute the long $T_1^{(sv)} = 38 \pm 7$ s to the simultaneous spin-valley flip between the lower ES and the GS. The two-orders-of-magnitude difference in relaxation rates for different read levels is striking. To validate our observations and rule out potential thermally activated and flicker noise origin of steps in Methods.

CONCLUSIONS

The notably long T_1 times, together with the demonstrated high-fidelity readout, present exciting opportunities for studying spin and valley physics at low and zero magnetic fields, where it holds particular significance as the energy splittings align with the capabilities of standard microwave equipment operating around 5 – 12 GHz. Performing such measurements in a device based on purified Carbon-12 graphene would allow for a platform free of hyperfine-induced decoherence. Additionally, the significantly weaker spin-mixing component of a spin-orbit coupling in BLG (~ 5 neV) [3, 30], compared to other established semiconducting platforms (60 neV for GaAs [31], 200 neV for Ge [32] and 110 neV for silicon metal-oxide-semiconductor [33]), suggests that it may not limit spin coherence times in BLG due to charge noise, one of the key factor constraining the performance in conventional platforms [1]. Furthermore, replacing the lossy amorphous aluminum oxide between gate layers with dangling-bond-free hBN could potentially reduce charge noise in BLG QD devices [34].

An open question remains regarding how to coherently manipulate the valley degree of freedom, since the valley magnetic moment is only coupled to the out-of-plane magnetic field. This problem can be addressed by utilizing spin-valley exchange interaction between the (2,0) and (1,1) orbital configurations in a double dot geometry. The resulting Kramers singlet-triplet qubit can be operated similarly to its spin analog [35, 36] leveraging the gate-tunability of the valley g -factor, as shown in the Supplementary Figure 4. Additionally, the readout of the Kramers singlet-triplet qubit can be achieved via Pauli spin-valley blockade [37]. Another approach to manipulating Kramers states relies on a presence of a finite valley mixing term $\propto \tau_x \Delta_{K+K^-}$ in the original QD Hamiltonian due to the breaking of translational symmetry [38]. As a result, one can drive spin-valley rotation by exploiting conventional electron spin resonance protocols (see Supplementary Figure 3) using antennas, micromagnets [1, 2] or utilizing the highly anisotropic effective g -factor in a curved BLG quantum dot [38], similar to carbon nanotubes [20, 39]. Independent of the magnitude of valley mixing, two-qubit gates between spin-valley qubits can be facilitated through exchange interactions, providing a robust roadmap for quantum information processing.

ACKNOWLEDGEMENTS

The authors thank Lin Wang, Guido Burkard and Joshua Folk for useful discussions. All authors acknowledge financial support by the European Graphene Flagship Core3 Project, H2020 European Research Council (ERC) Synergy Grant under Grant Agreement 951541, the European Innovation Council under grant agreement number 101046231/FantastiCOF, NCCR QSIT (Swiss National Science Foundation, grant number 51NF40-185902). K.W. and T.T. acknowledge support from the JSPS KAKENHI (Grant Numbers 21H05233 and 23H02052) and World Premier International Research Center Initiative (WPI), MEXT, Japan.

AUTHOR CONTRIBUTIONS STATEMENT

Corresponding authors

Correspondence and requests for materials should be addressed to A.D., H.D.

Author contributions

T.T. and K.W. grew the hBN. H.D. fabricated the device with inputs from M.M. and M.R.. A.D. acquired and analyzed the data with inputs from S.C, H.D, T.I. and K.E.. V.R. performed numerical simulations of the device. A.D. wrote the manuscript with inputs from all authors.

COMPETING INTERESTS

The authors declare no competing financial interests.

* adenisov@phys.ethz.ch

† hadrien.duprez@polytechnique.edu

- [1] G. Burkard, T. D. Ladd, A. Pan, J. M. Nichol, and J. R. Petta, Semiconductor spin qubits, *Rev. Mod. Phys.* **95**, 025003 (2023).
- [2] A. Chatterjee, P. Stevenson, S. De Franceschi, A. Morello, N. P. de Leon, and F. Kuemmeth, Semiconductor qubits in practice, *Nature Reviews Physics* **3**, 157 (2021).
- [3] R. Garreis, C. Tong, J. Terle, M. J. Ruckriegel, J. D. Gerber, L. M. Gächter, K. Watanabe, T. Taniguchi, T. Ihn, K. Ensslin, and W. W. Huang, Long-lived valley states in bilayer graphene quantum dots, *Nature Physics* **20**, 428 (2024).
- [4] L. M. Gächter, R. Garreis, J. D. Gerber, M. J. Ruckriegel, C. Tong, B. Kratochwil, F. K. de Vries, A. Kurzmam, K. Watanabe, T. Taniguchi, T. Ihn, K. Ensslin,

- and W. W. Huang, Single-shot spin readout in graphene quantum dots, *PRX Quantum* **3**, 020343 (2022).
- [5] L. Banszerus, S. Möller, K. Hecker, E. Icking, K. Watanabe, T. Taniguchi, F. Hassler, C. Volk, and C. Stampfer, Particle-hole symmetry protects spin-valley blockade in graphene quantum dots, *Nature* **618**, 51 (2023).
 - [6] E. McCann and M. Koshino, The electronic properties of bilayer graphene, *Reports on Progress in Physics* **76**, 056503 (2013).
 - [7] A. Knothe, L. I. Glazman, and V. I. Fal'ko, Tunneling theory for a bilayer graphene quantum dot's single- and two-electron states, *New Journal of Physics* **24**, 043003 (2022).
 - [8] A. Kormányos, V. Zólyomi, N. D. Drummond, and G. Burkard, Spin-orbit coupling, quantum dots, and qubits in monolayer transition metal dichalcogenides, *Phys. Rev. X* **4**, 011034 (2014).
 - [9] F. Borjans, D. M. Zajac, T. M. Hazard, and J. R. Petta, Single-spin relaxation in a synthetic spin-orbit field, *Phys. Rev. Applied* **11**, 044063 (2019).
 - [10] L. C. Camenzind, L. Yu, P. Stano, J. D. Zimmerman, A. C. Gossard, D. Loss, and D. M. Zumbühl, Hyperfine-phonon spin relaxation in a single-electron gas quantum dot, *Nature Communications* **9**, 3454 (2018).
 - [11] L. Wang, I. Meric, P. Y. Huang, Q. Gao, Y. Gao, H. Tran, T. Taniguchi, K. Watanabe, L. M. Campos, D. A. Muller, J. Guo, P. Kim, J. Hone, K. L. Shepard, and C. R. Dean, One-dimensional electrical contact to a two-dimensional material, *Science* **342**, 614 (2013).
 - [12] R. Krishnan, S. Biswas, Y.-L. Hsueh, H. Ma, R. Rahman, and B. Weber, Spin-valley locking for in-gap quantum dots in a MoS₂ transistor, *Nano Letters* **23**, 6171 (2023).
 - [13] A. Knothe and V. Fal'ko, Influence of minivalleys and berry curvature on electrostatically induced quantum wires in gapped bilayer graphene, *Phys. Rev. B* **98**, 155435 (2018).
 - [14] C. Tong, R. Garreis, A. Knothe, M. Eich, A. Sacchi, K. Watanabe, T. Taniguchi, V. Fal'ko, T. Ihn, K. Ensslin, and A. Kurzmann, Tunable valley splitting and bipolar operation in graphene quantum dots, *Nano Letters* **21**, 1068 (2021).
 - [15] C. L. Kane and E. J. Mele, Quantum spin hall effect in graphene, *Phys. Rev. Lett.* **95**, 226801 (2005).
 - [16] A. Kurzmann, Y. Kleeorin, C. Tong, R. Garreis, A. Knothe, M. Eich, C. Mittag, C. Gold, F. K. de Vries, K. Watanabe, T. Taniguchi, V. Fal'ko, Y. Meir, T. Ihn, and K. Ensslin, Kondo effect and spin-orbit coupling in graphene quantum dots, *Nature Communications* **12**, 6004 (2021).
 - [17] L. Banszerus, S. Möller, C. Steiner, E. Icking, S. Trelenkamp, F. Lentz, K. Watanabe, T. Taniguchi, C. Volk, and C. Stampfer, Spin-valley coupling in single-electron bilayer graphene quantum dots, *Nature Communications* **12**, 5250 (2021).
 - [18] L. Banszerus, K. Hecker, S. Möller, E. Icking, K. Watanabe, T. Taniguchi, C. Volk, and C. Stampfer, Spin relaxation in a single-electron graphene quantum dot, *Nature Communications* **13**, 3637 (2022).
 - [19] H. Duprez, S. Cances, A. Omahen, M. Masseroni, M. J. Ruckriegel, C. Adam, C. Tong, R. Garreis, J. D. Gerber, W. Huang, L. Gächter, K. Watanabe, T. Taniguchi, T. Ihn, and K. Ensslin, Spin-valley locked excited states spectroscopy in a one-particle bilayer graphene quantum dot, *Nature Communications* **15**, 9717 (2024).
 - [20] E. A. Laird, F. Pei, and L. P. Kouwenhoven, A valley-spin qubit in a carbon nanotube, *Nature Nanotechnology* **8**, 565 (2013).
 - [21] H. O. H. Churchill, F. Kuemmeth, J. W. Harlow, A. J. Bestwick, E. I. Rashba, K. Flensberg, C. H. Stwertka, T. Taychatanapat, S. K. Watson, and C. M. Marcus, Relaxation and dephasing in a two-electron ¹³C nanotube double quantum dot, *Phys. Rev. Lett.* **102**, 166802 (2009).
 - [22] F. Kuemmeth, S. Ilani, D. C. Ralph, and P. L. McEuen, Coupling of spin and orbital motion of electrons in carbon nanotubes, *Nature* **452**, 448 (2008).
 - [23] E. Icking, L. Banszerus, F. Wörtche, F. Volmer, P. Schmidt, C. Steiner, S. Engels, J. Hesselmann, M. Goldsche, K. Watanabe, T. Taniguchi, C. Volk, B. Beschoten, and C. Stampfer, Transport spectroscopy of ultraclean tunable band gaps in bilayer graphene, *Advanced Electronic Materials* **8**, 2200510 (2022).
 - [24] J. M. Elzerman, R. Hanson, L. H. Willems van Beveren, B. Witkamp, L. M. K. Vandersypen, and L. P. Kouwenhoven, Single-shot read-out of an individual electron spin in a quantum dot, *Nature* **430**, 431 (2004).
 - [25] A. Morello, J. J. Pla, F. A. Zwanenburg, K. W. Chan, K. Y. Tan, H. Huebl, M. Möttönen, C. D. Nugroho, C. Yang, J. A. van Donkelaar, A. D. C. Alves, D. N. Jamieson, C. C. Escott, L. C. L. Hollenberg, R. G. Clark, and A. S. Dzurak, Single-shot readout of an electron spin in silicon, *Nature* **467**, 687 (2010).
 - [26] C. B. Simmons, J. R. Prance, B. J. Van Bael, T. S. Koh, Z. Shi, D. E. Savage, M. G. Lagally, R. Joynt, M. Friesen, S. N. Coppersmith, and M. A. Eriksson, Tunable spin loading and T₁ of a silicon spin qubit measured by single-shot readout, *Phys. Rev. Lett.* **106**, 156804 (2011).
 - [27] D. Keith, S. K. Gorman, L. Kranz, Y. He, J. G. Keizer, M. A. Broome, and M. Y. Simmons, Benchmarking high fidelity single-shot readout of semiconductor qubits, *New Journal of Physics* **21**, 063011 (2019).
 - [28] S. Amasha, K. MacLean, I. P. Radu, D. M. Zumbühl, M. A. Kastner, M. P. Hanson, and A. C. Gossard, Electrical control of spin relaxation in a quantum dot, *Phys. Rev. Lett.* **100**, 046803 (2008).
 - [29] C. H. Yang, A. Rossi, R. Ruskov, N. S. Lai, F. A. Mohiyaddin, S. Lee, C. Tahan, G. Klimeck, A. Morello, and A. S. Dzurak, Spin-valley lifetimes in a silicon quantum dot with tunable valley splitting, *Nature Communications* **4**, 2069 (2013).
 - [30] S. Konschuh, M. Gmitra, D. Kochan, and J. Fabian, Theory of spin-orbit coupling in bilayer graphene, *Phys. Rev. B* **85**, 115423 (2012).
 - [31] J. R. Petta, H. Lu, and A. C. Gossard, A coherent beam splitter for electronic spin states, *Science* **327**, 669 (2010).
 - [32] D. Jirovec, P. M. Mutter, A. Hofmann, A. Crippa, M. Rychetsky, D. L. Craig, J. Kukucka, F. Martins, A. Ballabio, N. Ares, D. Chrastina, G. Isella, G. Burkard, and G. Katsaros, Dynamics of hole singlet-triplet qubits with large *g*-factor differences, *Phys. Rev. Lett.* **128**, 126803 (2022).
 - [33] T. Tanttu, B. Hensen, K. W. Chan, C. H. Yang, W. W. Huang, M. Fogarty, F. Hudson, K. Itoh, D. Culcer, A. Laucht, A. Morello, and A. Dzurak, Controlling spin-orbit interactions in silicon quantum dots using magnetic field direction, *Phys. Rev. X* **9**, 021028 (2019).
 - [34] J. I.-J. Wang, M. A. Yamoah, Q. Li, A. H. Karamlou, T. Dinh, B. Kannan, J. Braumüller, D. Kim, A. J.

- Melville, S. E. Muschinske, B. M. Niedzielski, K. Seraniak, Y. Sung, R. Winik, J. L. Yoder, M. E. Schwartz, K. Watanabe, T. Taniguchi, T. P. Orlando, S. Gustavsson, P. Jarillo-Herrero, and W. D. Oliver, Hexagonal boron nitride as a low-loss dielectric for superconducting quantum circuits and qubits, *Nature Materials* **21**, 398 (2022).
- [35] J. R. Petta, A. C. Johnson, J. M. Taylor, E. A. Laird, A. Yacoby, M. D. Lukin, C. M. Marcus, M. P. Hanson, and A. C. Gossard, Coherent manipulation of coupled electron spins in semiconductor quantum dots, *Science* **309**, 2180 (2005).
- [36] D. Jirovec, A. Hofmann, A. Ballabio, P. M. Mutter, G. Tavani, M. Botifoll, A. Crippa, J. Kukucka, O. Sagi, F. Martins, J. Saez-Mollejo, I. Prieto, M. Borovkov, J. Arbiol, D. Chrastina, G. Isella, and G. Katsaros, A singlet-triplet hole spin qubit in planar ge, *Nature Materials* **20**, 1106 (2021).
- [37] C. Tong, A. Kurzmann, R. Garreis, W. W. Huang, S. Jele, M. Eich, L. Ginzburg, C. Mittag, K. Watanabe, T. Taniguchi, K. Ensslin, and T. Ihn, Pauli blockade of tunable two-electron spin and valley states in graphene quantum dots, *Phys. Rev. Lett.* **128**, 067702 (2022).
- [38] K. Flensberg and C. M. Marcus, Bends in nanotubes allow electric spin control and coupling, *Phys. Rev. B* **81**, 195418 (2010).
- [39] F. Pei, E. A. Laird, G. A. Steele, and L. P. Kouwenhoven, Valley-spin blockade and spin resonance in carbon nanotubes, *Nature Nanotechnology* **7**, 630 (2012).
- [40] A. Mills, C. Guinn, M. Feldman, A. Sigillito, M. Gullans, M. Rakher, J. Kerckhoff, C. Jackson, and J. Petta, High-fidelity state preparation, quantum control, and readout of an isotopically enriched silicon spin qubit, *Phys. Rev. Appl.* **18**, 064028 (2022).
- [41] P. Stano and D. Loss, Review of performance metrics of spin qubits in gated semiconducting nanostructures, *Nature Reviews Physics* **4**, 672 (2022).
- [42] A. Denisov, V. Reckova, A. Cances, M. Ruckriegel, M. Masseroni, C. Adam, C. Tong, J. Gerber, W. Huang, K. Watanabe, T. Taniguchi, T. Ihn, K. Ensslin, and H. Duprez, Spin-valley protected kramers pair in bilayer graphene, ETH-Bibliothek [10.3929/ethz-b-000711208](https://doi.org/10.3929/ethz-b-000711208) (2025).
- [43] A. Kurzmann, M. Eich, H. Overweg, M. Mangold, F. Herman, P. Rickhaus, R. Pisoni, Y. Lee, R. Garreis, C. Tong, K. Watanabe, T. Taniguchi, K. Ensslin, and T. Ihn, Excited states in bilayer graphene quantum dots, *Phys. Rev. Lett.* **123**, 026803 (2019).

METHODS

Device fabrication

All the presented data were measured on a single device fabricated on a van der Waals heterostructure stacked by standard dry transfer techniques. The stack consists of a 35 nm thick top hBN layer, the Bernal BLG sheet, a 28 nm thick bottom hBN, and a graphite back gate layer. The ohmic contacts to the BLG are 1D edge contacts. To form QDs, we utilize the two overlapping layers of Cr/Au (3 nm/20 nm) metallic gates shown in Fig. 1a.

The upper gate layer consists of finger gates, 20 nm-wide and 60 nm apart. These gates are deposited on top of a 26 nm thick insulating aluminum oxide layer. The widths of the channels defined by the split gates are 40 nm for the left channel and 75 nm for the right channel, respectively. We tune the dot into the few-hole regime as shown in Fig. 1b. We attribute the set of parallel discrete steps to the boundaries of the regions of the charge stability diagram with a constant hole occupation $N_h = 0, 1, 2, \dots$ as indicated in the figure. We identify the first hole transition around $V_{P1} \approx 13$ V (marked by the red dot), as no charge transition line appears at higher plunger gate voltages. Additional lines with drastically different couplings to MS and P1 gates correspond to unintended dots formed due to nearby charge inhomogeneities.

By applying a large negative voltage $V_{BG} = -7.4$ V to the global back gate we induce a large displacement field ($D = -0.9$ V/nm) which opens a band gap in BLG on the order of 100 meV. This field allows us to significantly decouple the dot from the reservoirs, achieving tunneling rates to the leads of just tens of Hz.

Measurement setup

The sample is mounted on the mixing chamber of a Bluefors LD400 dilution refrigerator, which has a base temperature of 9 mK and an independently extracted electron temperature of around 30 mK. All the measurement and control electronics are located at room temperature and are connected to the device via 24 DC lines. Each line is low-pass filtered using RC filters mounted on the mixing chamber plate, with a time constant of approximately 10 μ s. For DC biasing of gates and ohmic contacts, we use in-house built low-noise voltage sources with a cutoff frequency of 7 Hz, except for the pulsing gate P1 line, which is left unfiltered and has a cutoff frequency of 1200 Hz. The DC plunger gate voltage V_{P1} is combined with the pulsing voltage V_{pulse} using a 2 M Ω /2.7 k Ω divider at room temperature. The sensor current is amplified using a built in-house current to voltage converter with a 10 M Ω feedback resistor, followed by a $\times 100$ analog voltage amplifier and an analog low-pass filter with a cutoff frequency of around 10 kHz. Sensor time traces are recorded using an NI-6251 data acquisition card with a sampling frequency of 20 kHz.

Elzerman sequence

We start the three-level single-shot readout sequence with the empty dot subjected to the ‘Load’ phase (see Fig. 1c): the pulse level shifts all three states below the Fermi energy E_F of the leads. A hole from the lead can tunnel into any of the three states with almost equal probability [19] of 1/3. During the ‘Load’ phase of du-

ration T_{load} , the sensor current drops abruptly, indicating that the dot has been filled, as shown in the typical time traces in Fig. 1d. In the following ‘Read’ phase (see Fig. 1c), the second pulse level puts the excited state of interest above E_F in the lead while the ground state stays below. If a hole remains in the excited state after loading and during the ‘Read’ phase without relaxing, then, at some random time governed by the tunneling-out rate, it will tunnel to the leads and thereafter the ground state of the dot will be occupied again through a tunneling-in process. This in-and-out tunneling manifests itself as a step in the sensor current shown in Fig. 1d (green trace). In contrast, no step is observed when the hole was initially loaded into the ground state, or when it relaxed before it could tunnel out during the ‘Read’ phase (blue trace). Once a hole arrives in the ground state, it blocks any further transitions since the number of resonant unoccupied lead states is exponentially suppressed by the low electron temperature $T_e \approx 30$ mK [19]. The final pulse level empties the dot by moving all states above E_F of the leads (see Fig. 1c), and after that, the sequence starts again.

Postselection of sensor traces

We digitize current sensor traces using the two-threshold procedure described in [19]. We divide the entire set of N digitized current traces into four groups, $N = (N_e, N_g, N_{\text{nl}}, N_{\text{er}})$. Here, N_{nl} is the number of traces where a hole was not loaded during the ‘Load’ phase. N_g is the number of traces with zero steps in the ‘Read’ phase, which we label as a hole being in the ground state. N_e is the number of traces with a single step during the ‘Read’ phase, which we define as a hole being in the excited state. N_{er} is for the rest of the traces, which we label as errors, as they exhibit multiple steps in the ‘Read’ phase. Extended Data Fig. 1 shows typical sensor cur-

rent traces for each group along with their digitized version. The typical proportions are as follows: 80.89% for the ground state (GS), 9.41% for the excited state (ES), 0.39% for combined errors, and 0.58% for traces that are not loaded. The two most common types of errors causing multiple step traces are digitization errors and random thermal/charge noise steps. The first is due to the fact that the sensor trace doesn’t exhibit enough points in both charge states to reliably determine the threshold for digitization. Thermal steps are exponentially suppressed by low electron temperature, while major charge jumps occur on a very long timescale of minutes and hours. We simply discard all error traces from the dataset, assuming that the errors are uncorrelated with whether the excited or ground state is occupied in the beginning of the ‘Read’ phase. Note that by discarding clearly excited state counts, however marked as thermal step errors in Extended Data Fig. 1, we underestimate the excited state probability.

Calculation of excited state probability

We perform relaxation time measurements in a regime with slow tunneling rates $\Gamma_{\text{out}} \approx \Gamma_{\text{in}} \sim 15$ Hz, which are comparable to the measured T_1 at certain magnetic fields. In this regime, the occupation of the excited state after the short loading times $T_{\text{load}} \sim \Gamma_{\text{in}}^{-1}$ is limited not by the relaxation but by the tunneling-in rate. Nevertheless, even for one of the shortest extracted $T_1 \approx 40$ ms, we demonstrate that the decay of the calculated renormalized excited state probability P^e can be fit by a simple exponent. We consider the state readout of two double-degenerate Kramers pairs at $B_{\parallel} = 900$ mT, as shown in Extended Data Fig. 2a. As established in previous measurements [9, 26], the total occupations of the excited, ground, and non-loaded states after the loading time T_{load} are

$$\begin{aligned} n^e(T_{\text{load}}) &= \frac{N_e}{N_e + N_g + N_{\text{nl}}} = \frac{\Gamma_{\text{in}}^e}{\Gamma_{\text{in}}^e + \Gamma_{\text{in}}^g - T_1^{-1}} e^{-T_{\text{load}} T_1^{-1}} \left(1 - e^{-T_{\text{load}} (\Gamma_{\text{in}}^e + \Gamma_{\text{in}}^g - T_1^{-1})} \right) \\ n^g(T_{\text{load}}) &= \frac{N_g}{N_e + N_g + N_{\text{nl}}} = \frac{(\Gamma_{\text{in}}^g - T_1^{-1}) \left(1 - e^{-T_{\text{load}} (\Gamma_{\text{in}}^e + \Gamma_{\text{in}}^g)} \right) + \Gamma_{\text{in}}^e \left(1 - e^{-T_{\text{load}} T_1^{-1}} \right)}{\Gamma_{\text{in}}^e + \Gamma_{\text{in}}^g - T_1^{-1}} \\ n^{\text{nl}}(T_{\text{load}}) &= 1 - n^e - n^g \end{aligned} \quad (1)$$

where Γ_{in}^e and Γ_{in}^g are tunneling-in rates to the excited and the ground state respectively. We extract the sum of tunneling-in rates $\Gamma_{\text{in}}^e + \Gamma_{\text{in}}^g = 4\Gamma_{\text{in}} = 57.6$ Hz and tunneling-out rate $\Gamma_{\text{out}}^e = \Gamma_{\text{out}}^g = \Gamma_{\text{out}} = 12$ Hz by fitting the exponential decay and rise of the average dot occupation during the ‘Load’ and ‘Empty’ phases respec-

tively, as shown in Extended Data Fig. 2a. During the ‘Read’ phase, we measure the excited states with efficiency [9, 26]:

$$n_{\text{RO}} = \frac{\Gamma_{\text{out}}^e}{T_1^{-1} + \Gamma_{\text{out}}^e} \left(1 - e^{-T_{\text{read}} (T_1^{-1} + \Gamma_{\text{out}}^e)} \right) \quad (2)$$

where T_{read} is the time spent in the ‘Read’ phase and Γ_{out}^e being the intrinsic tunneling rate.

The resulting full and renormalized probabilities are simply products of both efficiencies.

$$\begin{aligned} P_{\text{full}}^e(T_{\text{load}}) &= \frac{N_e}{N_e + N_g + N_{\text{nl}}} \cdot n_{\text{RO}} = n^e \cdot n_{\text{RO}} \\ P_{\text{renorm}}^e(T_{\text{load}}) &= \frac{N_e}{N_e + N_g} \cdot n_{\text{RO}} = \frac{n^e}{n^e + n^g} \cdot n_{\text{RO}} \end{aligned} \quad (3)$$

In Extended Data Fig. 2b, we plot the measured renormalized probability $P^e = N_e/(N_e + N_g)$ along with theoretical curves from (3), using $\Gamma_{\text{in}}^e = 22.2 \text{ Hz}$ and $T_1 = 41 \text{ ms}$. As expected, at short T_{load} , the full and renormalized occupations drastically differ. However, as long as $T_{\text{load}} > 60 \text{ ms} \approx 3/(\Gamma_{\text{in}}^e + \Gamma_{\text{in}}^g)$, the two curves match well, and their downward trend can be successfully approximated by the simple exponential function $P_{\text{exp}}^e(T_{\text{load}}) \sim e^{-T_{\text{load}}/T_1}$ as shown with the dashed line. With increasing relaxation time, the renormalized probability becomes closer to the exponent. The best least square weighted exponential fit of the experimental points yields $T_1 = 45 \pm 3 \text{ ms}$, which is within 10 percent of the value given by the correct renormalized probability expression.

Dark counts

In Extended Data Fig. 3, we rule out potential thermally activated and flicker noise origin (dark counts) of steps by comparing the step distribution at significantly different loading times $T_{\text{load}} = 0.2 \text{ s}$ and 12.8 s . The average of all the single-shot I_{sens} traces identified as the GS (purple) shows a flat behavior during the ‘Read’ phase. In contrast, the average of ESs (green) exhibits a bump that rises on a timescale of $1/\Gamma_{\text{out}}$ and decays within $1/\Gamma_{\text{in}}$ [25]. The exponential decrease in step density to zero, governed by the tunneling-out rate, allows us to eliminate the charge noise origin of the steps, as one would anticipate a constant distribution of random charge jumps over the ‘Read’ phase. Another potential source of false-positive counts could be thermally activated steps. Since we only count single steps, the distribution might appear similar. However, with average tunneling-in and -out times of $1/\Gamma_{\text{in/out}} = 75 \text{ ms}$ and a ‘Read’ duration of $T_{\text{read}} = 350 \text{ ms}$, we expect a Poissonian distribution $P(k) = \lambda^k e^{-\lambda}/k!$ for the probability of a certain number of tunneling events k , with an average of $\lambda = 4.7$. The probability of having a single step (corresponding to two tunneling events) is $P(k=2) \approx 10\%$, while the probability of having no step is $P(k=0) \approx 1\%$, meaning that the remaining 88% of shots should be discarded as errors. In fact, for $T_{\text{load}} = 0.2 \text{ s}$, we identify 45.9% of shots with a single step, 51.9% of shots with no steps, 0.9% as not-loaded shots, and only 1.3% as

multiple-step errors, effectively ruling out thermal activation as the origin of the steps.

Readout performance

For quantum information applications, it is crucial to identify the factors limiting the readout performance. We analyze 2000 single-shot traces to extract the histogram of the peak value of the sensor current during the ‘Read’ phase, as illustrated in the inset of Fig. 3b. The well-separated Gaussian peaks representing the detection of the GS and the ES, with a signal-to-noise ratio (SNR) of approximately 4.9, result in an electrical readout fidelity exceeding 99.9% [25, 27]. The negligible electrical readout error suggests that the readout performance is limited by the spin/valley-to-charge conversion [27]. We find that, despite the deliberate reduction of the tunneling rates, the observed notably long spin-valley relaxation time still just meets all the minimum requirements [27] for achieving a fault-tolerant 99% readout visibility threshold [40]: 1) a large energy splitting more than 13-times larger than electron temperature. In our experiment $\Delta_1 \approx 55 \mu\text{eV} \gtrsim 13k_{\text{B}}T \approx 52 \mu\text{eV}$. 2) a 100-times faster tunnelling-out time than relaxation time. In our experiment, $T_1^{(\text{sv})} = 30 \text{ s} \gtrsim 100/\Gamma_{\text{out}} = 8 \text{ s}$, and 3) a 12 times larger sampling rate for data acquisition than the reloading rate. In our experiment, $\Gamma_{\text{s}} = 10 \text{ kHz} > 12\Gamma_{\text{out}} = 150 \text{ Hz}$.

Ruling out pure spin relaxation

Here we explicitly ruling out the argument that the observed long spin-valley relaxation times could be interpreted as fully dominated by pure spin relaxation. Indeed, few seconds to almost-a-minute [10] spin T_1 times have also been observed both in silicon and GaAs quantum dots [41]. Moreover, previous studies indeed report strong power law dependencies [41], which could, at first sight, explain the drastic drop in relaxation times as we transition from the pure spin to the spin-valley blockade regime while simultaneously shrinking the energy splitting.

To eliminate this argument, in Extended Data Fig. 4 we plot the data from Fig. 1e as a function of the energy splitting between the first excited and the ground states. Additionally, we include the spin relaxation rate T_1^{-1} data at higher magnetic fields (1.5 – 3 T) from Gächter *et al.* [4], measured in an analogous weakly coupled ($\Gamma \sim 350 \text{ Hz}$) single QD BLG device using the same Elzerman technique. The energy splitting dependence of T_1 extracted from both experiments is best described by a power law, $T_1^{-1} \propto \Delta E^{2.5}$ (highlighted by the green solid line). The observed power is in line with $\propto \Delta E^{3-7}$, as seen in GaAs and silicon spin qubits, and originates

from a combination of electron-phonon relaxation and various spin mixing mechanisms such as hyperfine interaction, spin-orbit coupling, and spin-valley mixing [41]. In the case of BLG, neither spin-mixing mechanisms are well-known nor has any theoretical prediction for spin T_1 dependence on the magnetic field been made while considering the 2D nature of phonons. However, calculations for single-layer graphene show that the power law $T_1^{-1} \propto \Delta E^{2-4}$ should not differ much from the mentioned 3D platforms. Taking this into account, if we assume that long spin-valley relaxation is solely dominated by spin relaxation, the trend correlating spin and Kramers points reveals a remarkable power of $\propto \Delta E^{20}$ as marked by the dashed blue line, although fitting a power law on such a restricted energy range should be approached with caution. Hence, a more plausible explanation for such a drastic change in T_1 would be the dual protection afforded by simultaneous spin-valley blocking when operating within the Kramers doublet. The continuous connection between the spin-valley (blue dots) and spin (green dots) relaxation data points can be attributed to the finite valley mixing term. Indeed, even small values of $\Delta_{K+K-} < 2 \text{ neV} \sim 0.5 \text{ MHz}$ [3] can provide effective mixing, considering that our shortest loading times are in the tens of milliseconds. Additionally, the spin-or-valley relaxation channel data points align with the pure spin trend, indicating that valley relaxation is significantly longer than spin relaxation, in agreement with previous observations [3].

DATA AVAILABILITY

The data that support the findings of this study will be made available online through the ETH Research Collection [42] at <http://hdl.handle.net/20.500.11850/711208>. This includes raw data, analysis scripts, and plotting scripts for figures from the main text, Extended Data, and Supplementary Information.

Extended data

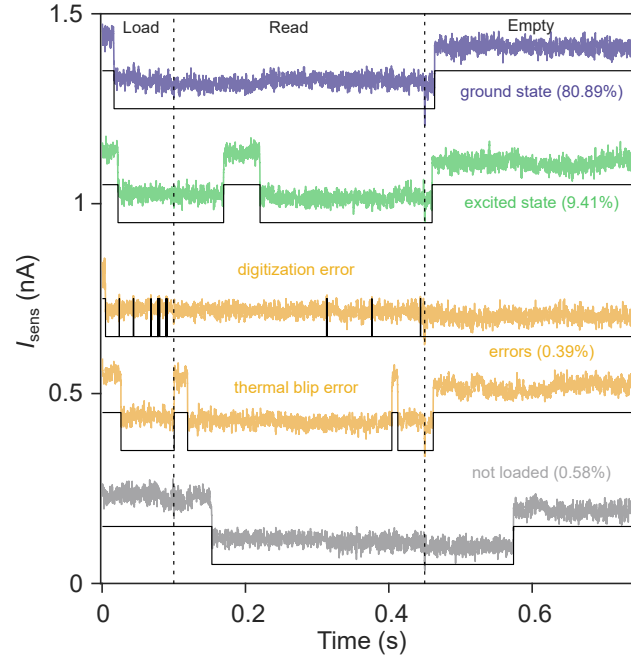


FIG. 1. **Postselection of sensor traces.** Typical time traces of the sensor current during the three-level pulse. Traces are shifted vertically with an equal offset of 0.3 nA. Black lines show the digitized versions of the traces. By analyzing the digitized signals, we group all traces into four groups: excited states (green), ground states (purple), errors (yellow), or not loaded states (gray). The percentage breakdown for each group is specified.

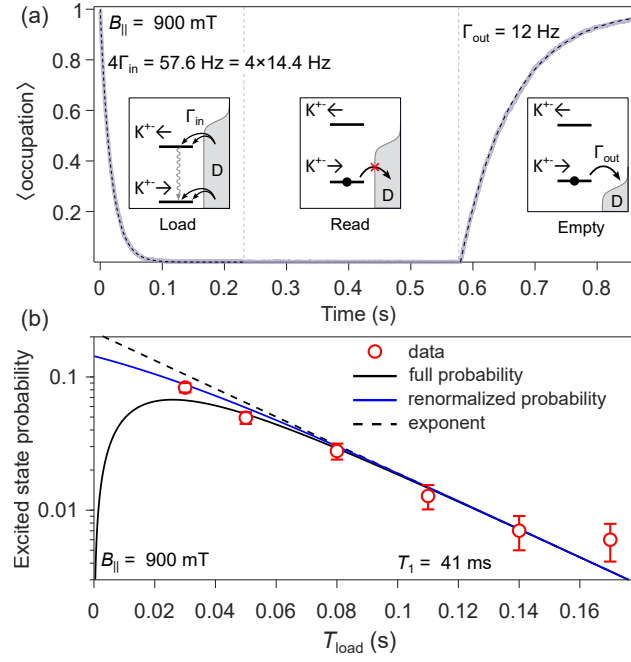


FIG. 2. **Calculation of excited state probability.** (a) Averaged over approximately 2000 shots, the occupation of the QD is shown as a function of time for $B_{\parallel} = 900$ mT and a loading time $T_{\text{load}} = 220$ ms, significantly longer than $T_1 = 41$ ms. Dashed lines represent exponential fits with outlined tunneling rates $\Gamma_{\text{in/out}}$. Energy diagrams sketch the standard three-level spin readout protocol. (b) The excited state probability is plotted against the loading time T_{load} . The dashed line shows an exponential fit with $T_1 = 41$ ms. The black line represents the full analytical probability, considering extracted tunneling rates and $T_1 = 41$ ms. The blue solid line depicts the renormalized probability after excluding all non-loaded shots.

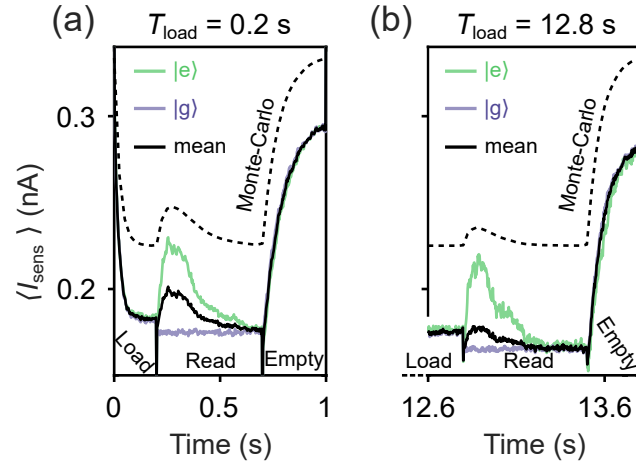


FIG. 3. **Dark counts.** Average of single-shot sensor current traces identified as the ES (green), the GS (purple), and the average of both (black) are shown for two very distinct loading times $T_{\text{load}} = 0.2$ s (a) and 12.8 s (b) measured in $B_{\perp} = 55$ mT. Dashed lines show the mean of the traces generated via Monte Carlo simulations. The vertical offset for the simulated data is introduced for clarity.

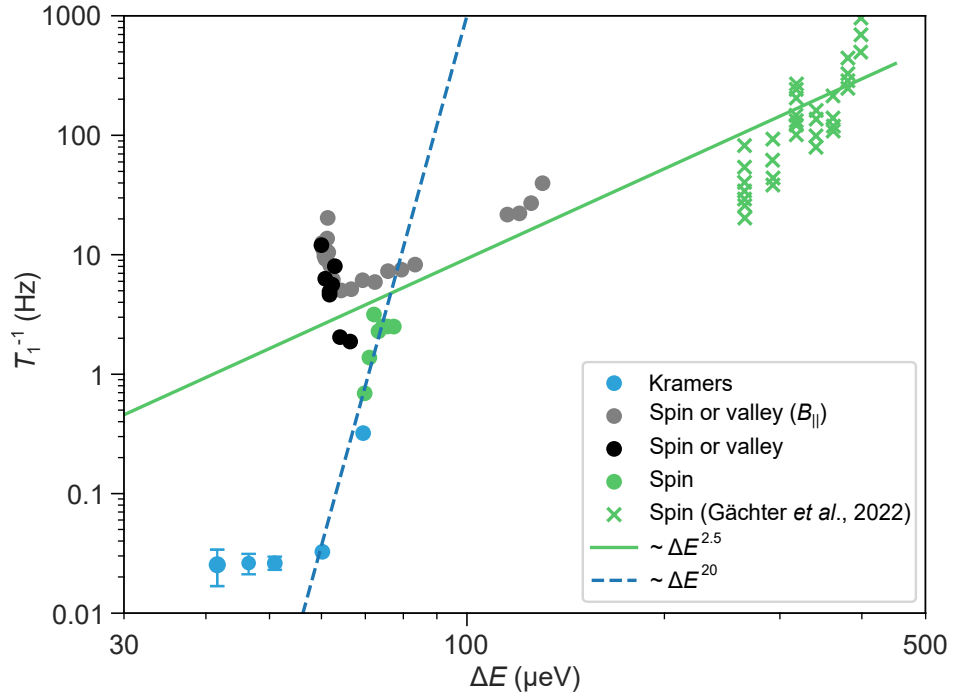


FIG. 4. **Ruling out pure spin relaxation.** Measured inverse relaxation time T_1^{-1} as a function of the energy splitting between relevant states. Circular markers of different colors correspond to different relaxation channels as outlined in the legend. Crosses correspond to the data points from [4], measured with the same Elzerman technique in a weakly coupled single BLG QD. Solid line shows the $\sim \Delta E^{2.5}$ trend in spin relaxation data. Dashed line shows $\sim \Delta E^{20}$, ruling out the assumption that Kramers qubit relaxation is dominated by the spin channel.

Supplementary Information

I. TUNNELING RATE SPECTROSCOPY

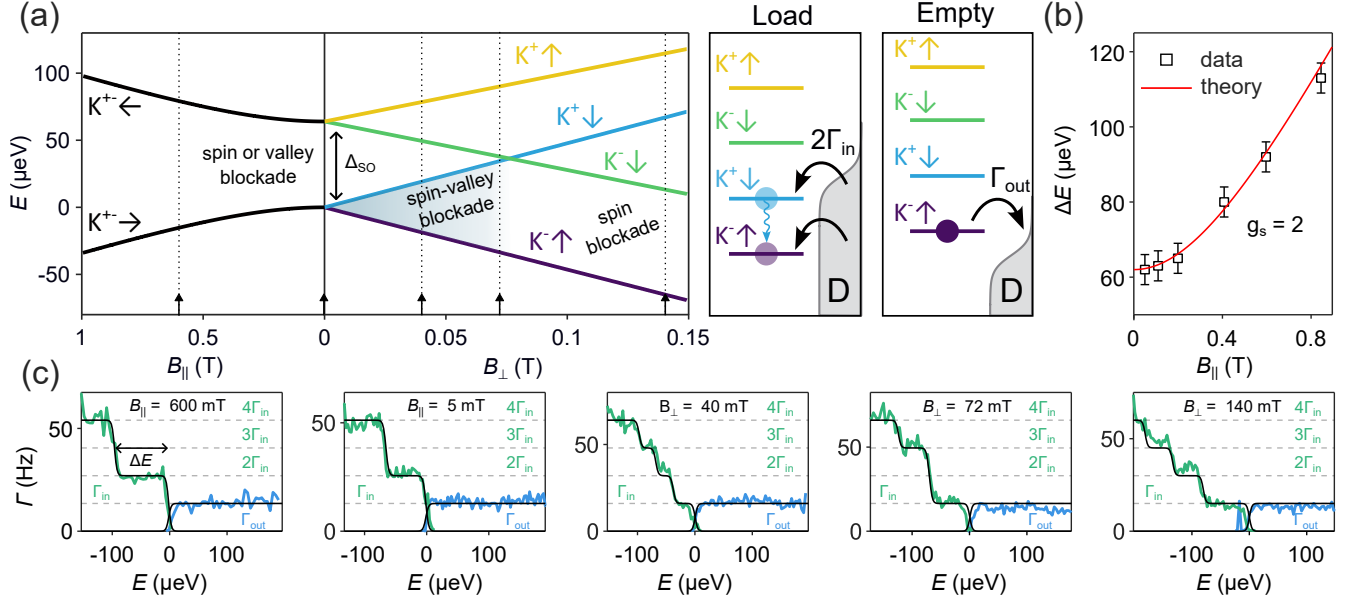


FIG. 5. **Tunneling rate spectroscopy.** (a) Energy spectrum of a single carrier in the BLG QD plotted as a function of in-plane and out-of-plane magnetic fields. Two-level pulse sequence for determining the in- and out-tunneling rates. The tunneling-in rate is proportional to the number of available energy states, while the tunneling-out rate is independent of the carrier's state. (b) Energy splitting between Kramers pairs ΔE is plotted as a function of in-plane magnetic field $B_{||}$. Solid red line is a theoretical curve with $g_s = 2$ and $\Delta_{SO} = 62 \mu\text{eV}$. Data points are presented as mean values \pm the thermal broadening $3.5k_B T_e/2 \approx 4 \mu\text{eV}$ of the Fermi-Dirac function. (c) Measured at different magnetic fields, tunneling-in (green) and -out (blue) rates are plotted as a function of the energy shift E relative to the GS. Black solid lines show theoretical curves with the sum of Fermi-Dirac distribution functions.

Tunneling rate spectroscopy technique assumes that all four states share the same orbital wave function. Consequently, the change in tunneling-in rates can be viewed as consecutive step functions, where the number of steps corresponds to the number of available states. To effectively measure the tunneling rates, we apply slow (1 – 3 Hz) periodic two-level square pulses which aim to ‘Load’ and ‘Empty’ the dot in each cycle as sketched in Fig. 5a. By measuring the waiting time t between the pulse and the actual tunneling event, we can extract both tunneling rates by fitting the exponential distribution $\sim \exp\{-\Gamma_{\text{in(out)}}t\}$. Additional details can be found in [19], where similar measurements were conducted on the same device. Fig. 5a shows the spectrum of the single hole in BLG QD as a function of in- and out-of-plane magnetic fields [7]. Close to zero magnetic field, two doubly-degenerate Kramers pairs manifest themselves as two plateaus in measured tunneling-in rate at approximately $\Gamma_{\text{in}} = 2\Gamma_{\text{out}}$ and $\Gamma_{\text{in}} = 4\Gamma_{\text{out}}$ as shown in Fig. 5c for $B_{||} = 5 \text{ mT}$. As expected, the tunneling-out rate is constant $\Gamma_{\text{out}} \approx 13 \text{ Hz}$ far away from the transition. The width of the $2\Gamma_{\text{in}}$ step at zero magnetic field corresponds to the spin-orbit gap Δ_{SO} . As we increase the in-plane field to $B_{||} = 600 \text{ mT}$, the degeneracy of the doublets stays the same, while the energy gap is increasing according to the in-plane polarization of the spin $\Delta = \sqrt{\Delta_{SO}^2 + (g_s \mu B_{||})^2}$. We fit the data with a sum of Fermi-Dirac distribution functions [19] with electron temperature $T_e = 25 \text{ mK}$ and $\Delta_{SO} = 62 \mu\text{eV}$ and $g_v = 14.5$. In contrast, the perpendicular magnetic field disrupts the degeneracy of the doublets. At $B_{\perp} = 40 \text{ mT}$, we notice four nearly evenly spaced energy steps, each with $\Gamma_{\text{in}} = \Gamma_{\text{out}}$. As we increase the field, at $B_{\perp} = 80 \text{ mT}$, two ESs intersect, leading to the merging of the second and third plateaus into a single one with $\Gamma_{\text{in}} = 3\Gamma_{\text{out}}$ as evident from the data. However, beyond the crossing point, at $B_{\perp} = 140 \text{ mT}$, the second plateau reappears with $\Gamma_{\text{in}} = 2\Gamma_{\text{out}}$. Note that we were only able to tune the dot to this textbook spectrum when the tunneling rates were as low as 10 – 20 Hz.

II. SPECTROSCOPY AROUND RELAXATION HOTSPOTS

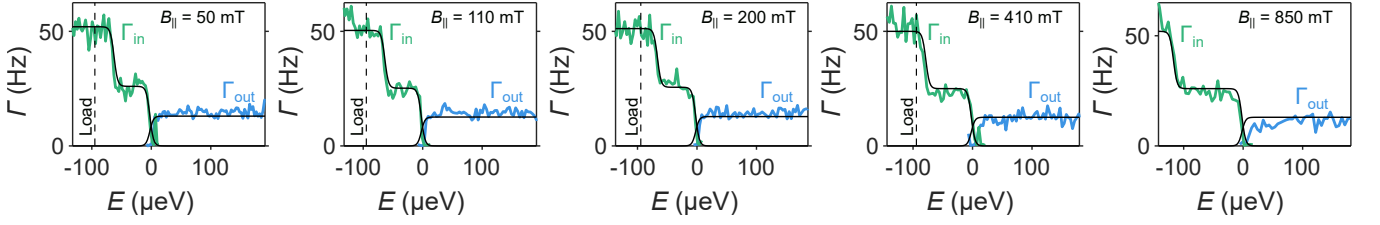


FIG. 6. **Tunneling rate spectroscopy around relaxation hotspot.** Measured at different in-plane magnetic fields $B_{||}$, tunneling-in (green) and -out (blue) rates are plotted as a function of the energy shift E relative to the GS. Black solid lines show analytical curves with the sum of Fermi-Dirac distribution functions, $g_s = 2$ and $\Delta_{SO} = 60 \mu\text{eV}$. The loading levels are marked with the dashed lines.

We noticed a sharp but rather shallow (2-3 times drop) hotspot in the measured T_1 around $B_{||} \approx 110 \text{ mT}$. In Fig. 6, we show the results of the tunneling rate spectroscopy around this point. As expected, all tunneling-in rate curves exhibit a similar two-step behavior as a function of the energy shift E in respect to the Fermi level in the leads. The width of the first step is defined by the splitting between two Kramers pairs and matches well with the theoretical predictions $\Delta E = \sqrt{\Delta_{SO}^2 + (g_s \mu_B B_{||})^2}$, where $\Delta_{SO} = 60 \mu\text{eV}$ and $g_s = 2$. The only thing we can point out at $B_{||} = 110 \text{ mT}$ (right on the hotspot) is a sign of a higher excited state emerging as an additional step in Γ_{in} at $E < -100 \mu\text{eV}$. However, this state is lying higher than the loading level, outlined by the dashed line, and should not contribute to the measurements.

III. COHERENT MANIPULATION OF THE KRAMERS STATES

A. Kramers singlet-triplet qubit

For a double quantum dot with a single carrier in each dot (1,1), the ground state is any combination of the following 4 states: $|K^+ \downarrow, K^+ \downarrow\rangle$, $|K^- \uparrow, K^- \uparrow\rangle$, $|K^+ \downarrow, K^- \uparrow\rangle$, $|K^- \uparrow, K^+ \downarrow\rangle$.

In the singlet-triplet basis:

$$\begin{aligned} |A\rangle(1,1) &= \frac{1}{\sqrt{2}}(|K^+ \downarrow, K^- \uparrow\rangle - |K^- \uparrow, K^+ \downarrow\rangle) \\ |B_0\rangle(1,1) &= \frac{1}{\sqrt{2}}(|K^+ \downarrow, K^- \uparrow\rangle + |K^- \uparrow, K^+ \downarrow\rangle) \\ |B_+\rangle(1,1) &= |K^+ \downarrow, K^+ \downarrow\rangle \\ |B_-\rangle(1,1) &= |K^- \uparrow, K^- \uparrow\rangle \end{aligned}$$

In the case of two-particles in a single dot, the ground state at $B=0$ has been shown to be a triple-degenerate valley-singlet, spin-triplet state [43]:

$$\begin{aligned} |S^v T_0^s\rangle(2,0) &= \frac{1}{2}(|K^+ \uparrow, K^- \downarrow\rangle - |K^- \downarrow, K^+ \uparrow\rangle + |K^+ \downarrow, K^- \uparrow\rangle - |K^- \uparrow, K^+ \downarrow\rangle) \\ |S^v T_+^s\rangle(2,0) &= \frac{1}{\sqrt{2}}(|K^+ \uparrow, K^- \uparrow\rangle - |K^- \uparrow, K^+ \uparrow\rangle) \\ |S^v T_-^s\rangle(2,0) &= \frac{1}{\sqrt{2}}(|K^+ \downarrow, K^- \downarrow\rangle - |K^- \downarrow, K^+ \downarrow\rangle) \end{aligned}$$

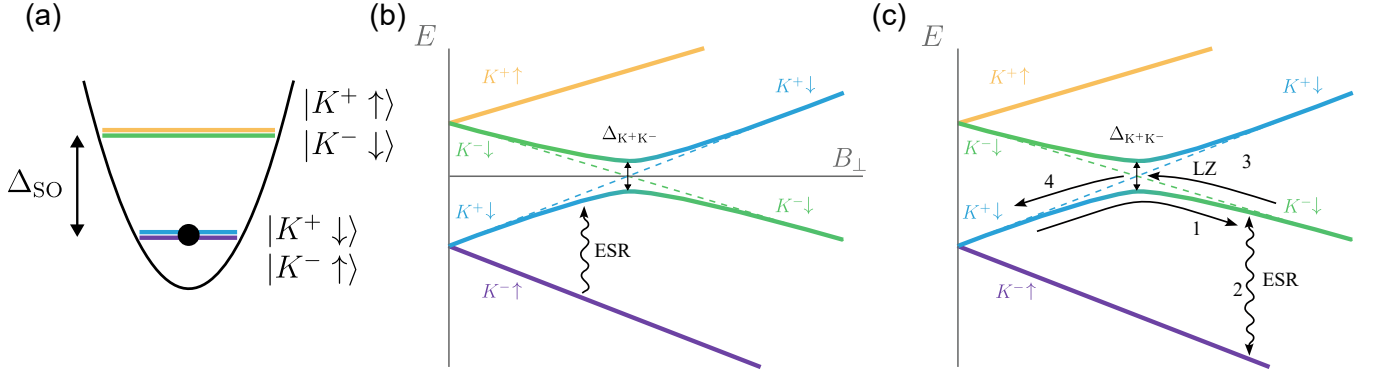


FIG. 7. **Kramers qubit manipulation based on valley-mixing.** (a) Single carrier QD in BLG. (b) Energy dispersion of a single carrier in BLG QD in the presence of a finite intervalley scattering term $\Delta_{K^+K^-}$. The Kramers qubit can be driven via Electric Spin Resonance (ESR).

As we see, only $|S^v T_0^s\rangle(2, 0)$ and $|A\rangle(1, 1)$ (highlighted in blue) can be coupled by interdot tunnelling in the assumption that the spin and valley quantum numbers are conserved during the tunnelling process. One can show that the resulting tunneling Hamiltonian, spanned by the Kramers singlet $|A\rangle(1, 1)$ and unpolarized triplet $|B_0\rangle(1, 1)$ states is similar to its spin analog [35].

B. Loss-DiVincenzo Kramers qubit via finite intervalley mixing

In the presence of a finite valley scattering term, the operation of the Kramers qubit is relatively straightforward, as theoretically described in [38] as well as experimentally demonstrated on carbon nanotubes by Laird et al. [20]. Unlike CNTs, however, $\Delta_{K^+K^-} < 0.5$ MHz in BLG is significantly suppressed due to the low long- and short-range disorder which would otherwise cause large-momentum scattering. Following the theoretical work on CNTs, in a presence of the finite intervalley mixing, we can project our original single particle Hamiltonian:

$$H = -\frac{1}{2}(\tau_z \Delta_{\text{SO}} \sigma_z + \tau_x \Delta_{K^+K^-}) + g_s \mu_B \vec{\sigma} \cdot \vec{B} + \tau_z g_v \mu_B B_{\perp}$$

onto the lowest two eigenstates (Kramers pair) yielding an effective spin-1/2 system:

$$H^* = \frac{1}{2} \mu_B (s_z g_{\perp} B_{\perp} + s_x g_{\parallel} B_{\parallel}), \quad \text{where } g_{\perp} = g_s + 2g_v \frac{\Delta_{\text{SO}}}{\sqrt{\Delta_{\text{SO}}^2 + \Delta_{K^+K^-}^2}}, \quad g_{\parallel} = 2g_s \frac{\Delta_{K^+K^-}}{\sqrt{\Delta_{\text{SO}}^2 + \Delta_{K^+K^-}^2}}$$

Here, s_x and s_z are spin Pauli matrices, and B_{\parallel} represents the in-plane magnetic field parallel to the BLG plane. The above Hamiltonian allows for the use of conventional ESR to drive (see Fig. 7b) the qubits, either by employing a microwave antenna or micromagnet, or by utilizing the geometric bends of the QD, as demonstrated in CNTs [20]. Note that the desirable in-plane g-factor component g_{\parallel} , is expected to vanish as $\Delta_{K^+K^-} \rightarrow 0$. This originates from the mixing of the first $K^+ \downarrow$ and second $K^- \downarrow$ excited states as we approach the anticrossing point, as shown in Fig. 7b. In BLG, $\Delta_{K^+K^-} \ll \Delta_{\text{SO}}$, so $g_{\parallel} \ll g_s$ and as a result, Rabi frequencies are expected to be significantly slower than those of spin Loss-DiVincenzo qubits [1].

C. Valley qubit via finite intervalley mixing

Another interesting possibility is to drive a pure valley qubit using a non-adiabatic pulsing across the Landau-Zener transition shown in Fig. 7c. Fast pulsing across the magnetic field axis can be achieved by leveraging the tunable valley g-factor. One possible protocols is illustrated in Fig. 7c:

1. Adiabatically drive the system across the LZ transition, to obtain a quantum state encoded solely in the spin, and perform Elzerman readout to initialize the spin in the ground state.

2. Apply a spin π -pulse using ESR drive to excite the carrier into $K^- \downarrow$ state.
3. Non-adiabatically pulse close to the anticrossing and wait for Larmor precession of the valley with rate equal to $\Delta_{K^+K^-}$.
4. Non-adiabatically pulse far from the anticrossing and perform energy-selective readout between $K^- \downarrow$ and $K^+ \downarrow$ states.

IV. GATE-TUNABLE VALLEY MAGNETIC MOMENT

The unique property of BLG is a gate-tunable valley g -factor, which allows electrical driving of the Kramers singlet-triplet states as well as adiabatic sweeps across the intervalley (anti)crossing. Here we experimentally demonstrate the tunability of g_v in the range from approximately 10 to 40 by simply varying the split-gate voltage. In Fig. 8 we measured the transition between 4 and 5 electrons in the QD, which behave similarly to the 0-to-1 transition, as 4 carriers form a full orbital shell. We did not observe this effect for the 0-to-1 transition within the range of split-gate voltages where the excited states of the dot are still resolvable. We attribute this to the fact that a quantum dot with 4 electrons is inherently larger than one starting with 0 electrons, and the size is what defines the valley magnetic moment [14].

In Fig. 8a, a Coulomb diamond is measured via direct current through the QD (high tunnelling rates). Finite-bias spectroscopy in Fig. 8b reveals the canonical single-particle energy spectrum as a function of the out-of-plane magnetic field, including two Kramers pairs. At fixed perpendicular magnetic field $B_\perp = 75$ mT, we track the energy splitting (red arrow in Fig. 8b) between $K^- \downarrow$ (green) and $K^+ \downarrow$ (blue) states as a function of split-gate voltage as shown in Fig. 8c. To directly measure the energy splitting, we sweep the bias voltage rather than the plunger gate, avoiding the need to separately measure the lever arm for each split-gate voltage. We can clearly observe the two excited states moving closer together and eventually crossing as the split-gate voltage is slightly increased (1.5 mV). This is directly related to the change of valley g -factor and moving of the crossing point between $K^- \downarrow$ (green) and $K^+ \downarrow$ (blue) states to higher magnetic fields in Fig. 8b (from 30 mT to 115 mT). The position of this crossing is defined only by the spin-orbit gap Δ_{SO} and valley g -factor g_v , while we ensure that the SO gap remains unchanged as a function of the split-gate voltage. This tunability enables nonadiabatic pulsing across the crossing point using electrical signals as well as ESR-like driving of the singlet-triplet qubit. Since the split-gate also influences the transition in plunger gate voltage, we virtually compensate for the plunger gate voltage to stay always around the the transition in Fig. 8c. This linear compensation is responsible for non-monotonic trend of excited state lines.

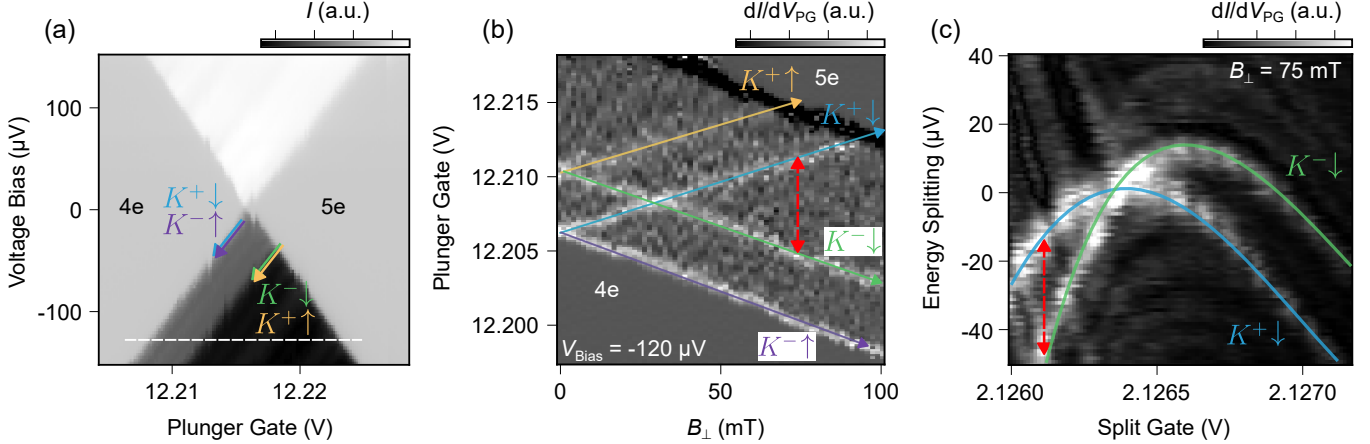


FIG. 8. **Tunable valley magnetic moment.** (a) The Coulomb diamond measured in the direct current through the quantum dot (QD) between the 4-to-5 electrons transition. The white dashed line indicates the bias voltage used for spectroscopy in a magnetic field. (b) Finite-bias spectroscopy as a function of the out-of-plane magnetic field shows the canonical spectrum. (c) The energy splitting between the first and second excited states is presented as a function of the split gate, measured at a fixed magnetic field of $B_\perp = 75$ mT. The reverse crossing of the states indicates the high tunability of the valley g -factor. Solid lines are provided as guides for the eye.

V. MONTE CARLO SIMULATIONS

A. Single-shot readout in a three-state quantum dot

In our simulation, we considered the quantum dot to be a 3-level system, with ground state, first excited state, and second excited state. The whole process of readout is divided into 4 parts - the loading stage, the waiting stage, the measurement stage, and the unloading stage.

In the loading stage, a charge carrier is loaded into the quantum dot. Because all the 3 states are well below the electrochemical potential of the leads, we assume that the charge carrier has an equal chance of ending up in either one of the 3 states.

If the charge carrier ends up in the ground state, it will remain there during the waiting stage. If the charge carrier is in one of the excited states, it might relax to a lower-energy state.

In the measurement stage, the energy level of the states is moved up by applying a voltage pulse. If the charge carrier is in the ground state, it may tunnel out. If it is in the first excited state, it may either tunnel out or relax to the ground state, and if it is in the second excited state, it may tunnel out, relax to the ground state, or relax to the first excited state. If the dot is empty at any point during the measurement stage, another charge carrier from the leads may fill either one of the 3 states, however, this time with different probabilities.

In the unloading stage, the energy level of the states is moved up way above the electrochemical potential of the leads, which causes the charge carrier to tunnel out from the quantum dot.

B. Probability of tunneling

All tunneling processes mentioned in the section above are probabilistic and described through tunneling rates. In the loading stage, we use tunneling rate $3\Gamma_{\text{in},0}$, because the electron can tunnel into either one of the 3 states. In the unloading stage, we use tunneling rate $\Gamma_{\text{out},0}$. In the simulation, we used the value (taken from the experiments) $\Gamma_{\text{in},0}=\Gamma_{\text{out},0} = 15 \text{ Hz}$.

In the measurement stage, the tunneling rate can be calculated using Fermi-Dirac distribution:

$$\Gamma_{\text{in/out}} = \frac{\Gamma_{\text{in/out},0}}{1 + e^{-\frac{E}{k_B T}}}, \quad (\text{S4})$$

where T is temperature (in the simulation we used value $T = 25 \text{ mK}$), k_B is the Boltzmann constant and E is the energy of the given state, assuming that the electrochemical potential of the leads corresponds to $E = 0$. We can notice that if the energy level of the given state is a bit below the electrochemical potential of the leads, the tunneling rate Γ_{in} is much larger than Γ_{out} and therefore it is more probable for a charge carrier to tunnel in than the opposite situation.

To calculate the probability of a charge carrier tunneling either in or out of the dot, we need to use Bayes' theorem. It states that the conditional probability of an event A happening while event B is true can be calculated using the following equation:

$$P(A|B) = \frac{P(B|A) \cdot P(A)}{P(B)}. \quad (\text{S5})$$

We can apply this theorem to calculate the probability of the dot getting occupied in time interval $[t, t + \Delta t]$, provided that the dot has been empty before that, in time interval $[0, t]$:

$$\begin{aligned} & P(\text{dot got occupied in } [t, t + \Delta t] | \text{dot was empty in } [0, t]) = \\ &= \frac{P(\text{dot got occupied in } [t, t + \Delta t]) \cdot P(\text{dot was empty in } [0, t] | \text{dot got occupied in } [t, t + \Delta t])}{P(\text{dot was empty in } [0, t])} \\ &= \frac{\int_t^{t+\Delta t} \Gamma e^{-\Gamma t} dt}{1 - \int_0^t \Gamma e^{-\Gamma t} dt} = \frac{e^{-\Gamma t} - e^{-\Gamma(t+\Delta t)}}{e^{-\Gamma t}} = 1 - e^{-\Gamma \Delta t}. \end{aligned} \quad (\text{S6})$$

In the calculation, we used the fact that the probability density of a tunneling event at a time t is given by

$$p(t) dt = \Gamma e^{-\Gamma t} dt. \quad (\text{S7})$$

In our simulation, we discretized the whole readout process, with a time step $t_{\text{step}} = 0.0005$ s. In each step, we generate a random number from 0 to 1 and calculate the probability given by equation (S6). If the randomly generated number is smaller than the calculated probability, the given tunneling event occurs.

VI. CHARGE STABILITY DIAGRAM

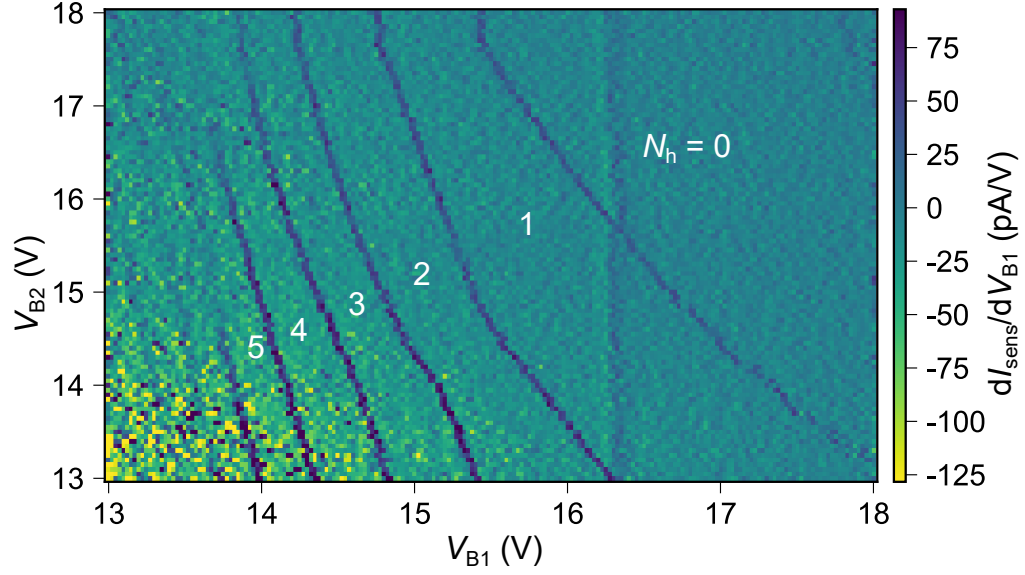


FIG. 9. **Barrier-barrier charge stability diagram.** Additional charge stability diagram. Sensor current derivative as a function of the barrier gate voltages. N_h indicates the number of hole carriers inside the QD.